Increasing river alkalinity slows ocean acidification in the northern Gulf of Mexico

Fabian A. Gomez[1,2], Rik Wanninkhof[2], Leticia Barbero[3,2], Sang-Ki Lee[2]

[1]Northern Gulf Institute, Mississippi State University, Starkville, Mississippi, USA.

[2]NOAA Atlantic Oceanographic and Meteorological Laboratory, Miami, Florida, USA.

[3]Cooperative Institute for Marine and Atmospheric Studies, University of Miami, Miami, Florida, USA.

Corresponding author: Fabian A. Gomez (fabian.gomez@noaa.gov)

Key Points:

- We simulated the spatiotemporal variability of ocean acidification progression over the Gulf of Mexico during 1981-2014.

- Model results showed positive trends in the surface ocean alkalinity, salinity, and temperature influencing acidification trends.

- Increasing Mississippi river alkalinity substantially lessened the ocean acidification progression on the northern Gulf of Mexico shelf.

17 **Abstract**

18 Ocean acidification (OA) progression is affected by multiple factors, such as ocean warming,

19 biological production, and runoff. Here we used an ocean-biogeochemical model to assess the

20 impact of river runoff and climate variability on the spatiotemporal patterns of OA in the Gulf of

21 Mexico (GoM) during 1981-2014. The model showed the expected pH and aragonite saturation

22 state (Ω_{Ar}) decline, due to the increase in anthropogenic carbon, with trends close to values

23 reported for the Subtropical North Atlantic. However, significant departures from the basin-

24 averaged pattern were obtained in part of the northern GoM shelf, where pH and Ω_{Ar} increased.

25 Model sensitivity analyses showed that OA progression was counteracted by enhanced alkalinity

26 from the Mississippi-Atchafalaya River System. Our findings highlight that river alkalinity is a

27 key driver of carbon system variability in river-dominated ocean margins and emphasize the need

28 to quantify riverine chemistry to properly assess acidification in coastal waters.

29 **Plain Language Summary**

30 Although ocean acidification (OA) is mainly driven by the ocean uptake of anthropogenic carbon

31 dioxide from the atmosphere, multiple factors influence its temporal progression, including

32 changes in ocean temperature, biological processes, and river discharge. Here we used numerical

33 model outputs to describe historical OA trends across the Gulf of Mexico (GoM) and identify the

34 main drivers of its spatial variability. We showed that changes in river runoff slowed OA over the

35 northern GoM coast. This was mainly due to an increasing Mississippi river alkalinity

36 concentration, a property related to the water capacity to neutralize acidification. Our results show

37 the importance of alkalinity changes to quantify OA progression in the GoM.

38 **1 Introduction**

39   Ocean acidification (OA), induced by the ocean uptake of atmospheric anthropogenic CO_2,

40 is affecting global ocean carbon chemistry, leading to a sustained decline in pH, along with an

41 increase in dissolved inorganic carbon (DIC), partial pressure of CO_2 (pCO_2), and calcium

42 carbonate solubility, the latter usually tracked as a decline in aragonite saturation state (Ω_{Ar})

43 (Doney et al., 2009; Gruber et al., 2019). These changes in carbon chemistry are negatively

44 impacting marine species and ecosystems. The most obvious impacts are associated with decreased

45 calcification rates in calcifying organisms, such as corals and shellfish, which results in reduced

46 individual growth and survival (e.g., Hoegh-Guldberg et al., 2007; Waldbusser et al., 2015). OA

47 is a major environmental stressor, which is expected to produce significant changes in marine

48 community structure and the availability of marine resources (Ekstrom et al., 2015; Cross et al.,

49 2019; Doney et al., 2020).

50 Datasets with records extending two or more decades have revealed long-term pCO_2

51 increases consistent with the increase in atmospheric CO_2, but variability is evident across regions

52 (Bates et al., 2014; Lauvset et al., 2015). Major departures from the anthropogenic CO_2-driven

53 changes can be expected in coastal regions, where variability in biological production, coastal

54 currents, temperature, and salinity are more likely to impact carbon chemistry trends (Cai et al.,

55 2011; Turi et al., 2016; Laruelle et al., 2018; Salisbury & Jönsson, 2018). This is particularly true

56 in river dominated ocean margins where the chemistry of river discharge directly influences the

57 ability of coastal waters to counteract acidification (Duarte et al., 2013,). Therefore, sustained

58 observational programs and modeling are required to identify OA progression and causes at

59 regional levels, so that ecosystem and socioeconomic vulnerabilities to OA can be assessed.

60 The Gulf of Mexico (GoM) hosts large spatiotemporal variability in its physical and

61 biogeochemical patterns and is significantly influenced by the Loop Current and the Mississippi-

62 Atchafalaya River System (MARS). The Loop Current transports warm and oligotrophic waters

63 from the Caribbean Sea, and largely defines water properties in the open GoM (Muller-Karger et

64 al., 2015; Damien et al., 2018). The MARS delivers large freshwater and nutrients fluxes to the

65 northern GoM shelf, strongly modulating regional salinity and biochemistry patterns (Dagg &

66 Breed, 2003; Rabalais et al., 2007). A series of observational studies have documented the

67 dominant spatial patterns and seasonal variability of pCO_2 and other carbon system variables in

68 the GoM (e.g., Lohrenz et al., 2018; Wang et al., 2013; Wanninkhof et al., 2015; Hu et al., 2015,

69 2018). However, interannual to multi-decadal variability remains poorly examined due to the lack

70 of sufficiently long time-series capable of discriminating OA trends from natural variability.

71 High-resolution ocean-biogeochemical models can assist in filling observational gaps by

72 describing and attributing ocean chemistry variability over time. Therefore, they are particularly

73 valuable tools for assessing the historical progression of OA and other low-frequency processes

74 that impact the carbon cycle. In a recent study, Gomez et al. (2020) configured and validated an

75 ocean-biogeochemical model for the GoM, examining dominant seasonal patterns in pCO_2 and

76 Ω_{Ar}. For the present study, we used the same model to investigate OA progression. We derived

77 long-term trends for OA indicators during 1981-2014 and performed sensitivity analyses to

78 examine the influence of river runoff and climate variability on OA progression.

79 **2 Methods**

80   We used the ocean-biogeochemical model described and validated in Gomez et al. (2018,

81 2020), which contains 16 state variables, including two inorganic carbon system variables: total

82 alkalinity (TA) and DIC. The ocean-biogeochemical model was implemented in the Regional

83 Ocean Model System (ROMS, Shchepetkin et al., 2005), with a horizontal resolution of ~8 km

84 and 37 sigma-coordinate vertical levels. A third order upstream scheme and a fourth order Akima

85 scheme were used for horizontal and vertical momentum, respectively. A multidimensional

86 positive definite advection transport algorithm (MPDATA) was used for tracer advection, while a

87 Mellor and Yamada 2.5-level closure scheme was used to resolve vertical turbulence. The initial

88 and open boundary conditions were derived from a 25 km horizontal resolution model for the

89 North Atlantic (Liu et al., 2015). Surface fluxes of momentum (6-hour resolution), heat (daily),

90 and precipitation (monthly) were derived from the European Centre for Medium Range Weather

91 Forecasts reanalysis product ERA-Interim (Dee et al., 2011) using a bulk flux parameterization.

92 River discharge, nutrients, TA, and DIC data were obtained from the U.S. Geological Survey for

93 rivers in the U.S. and derived from scientific literature for Mexican rivers (He et al. 2011; Muñoz-

94 Salinas & Castillo, 2015; Martínez-López & Zavala-Hidalgo, 2009). We prescribed a time-

95 evolving monthly series of freshwater discharge for 28 river sources in the U.S., and a

96 climatological discharge for 10 rivers in the U.S. and 11 rivers in Mexico. Due to the lack of

97 continuous long-term records, the time evolving concentration of nutrients, TA, and DIC were

98 prescribed for only the Mississippi and Atchafalaya rivers, while long-term climatological values

99 were prescribed for the other river sources. The partial pressure of atmospheric CO_2 (pCO_{2air}) was

100 prescribed as a continuous nonlinear function (using a third-degree polynomial expression plus

101 four harmonics) adjusted to the monthly pCO_{2air} series from the Mauna Loa Observatory.

102   In addition to the model hindcast, we also conduct two experiments to evaluate the OA

103 progression sensitivity to river runoff changes: the climatological MARS chemistry experiment

104 (CLM_MC) and the climatological rivers experiment (CLM_RIV). In CLM_MC, we used

105 monthly climatological values for the MARS's chemistry (nutrients, DIC, and TA). In CLM_RIV,

106   we used climatological river discharge values for all rivers, as well as the climatological chemistry

107   for the MARS. The influence of MARS's time evolving chemistry on OA was obtained from the

108   difference between the CLM_MC and hindcast trends, and the added impact of time evolving river

109   discharges and time-evolving MARS chemistry from the difference between the CLM_RIV and

110   hindcast trends. Hence, the difference between the CLM_MC and CLM_RIV trends provided an

111   estimate of the discharge variability impacts on OA. Finally, to evaluate the influence of climate

112   variability on the OA patterns, we conducted the climatological forcing experiment

113   (CLM_FORC), where we prescribed climatological patterns for rivers, surface fluxes and the open

114   boundary conditions at the southern and eastern edges of the model domain. The only exceptions

115   were pCO_{2air} and the open boundary conditions for DIC, which varied as in the model hindcast

116   (following Turi et al., 2016). The climate-variability impact was derived from the difference

117   between the CLM_FORC and hindcast trends.

118   Monthly outputs of surface DIC (sDIC), surface TA (sTA), sea surface salinity (SSS), and

119   sea surface temperature (SST) were used to derive simulated in situ patterns of three OA indicators:

120   pCO_2, pH, and Ω_{Ar}. To this effect, we used the CO2SYS program for CO_2 System Calculations

121   (van Heuven et al., 2011). A simple linear regression was used to calculate the trends from the

122   model's monthly anomalies for each variable of interest. Monthly outputs with the monthly

123   climatological mean of 1981-2014 removed (deseasonalized) were referred to as anomalies.

124   We used a first order Taylor series to decompose the surface pCO_2, pH, and Ω_{Ar} variability

125   into their four driver's components:

126   $$\Delta\varphi \approx \frac{\partial\varphi}{\partial sDIC} \cdot \Delta sDIC + \frac{\partial\varphi}{\partial sTA} \cdot \Delta sTA + \frac{\partial\varphi}{\partial SSS} \cdot \Delta SSS + \frac{\partial\varphi}{\partial SST} \cdot \Delta SST \quad \textbf{(1)}$$

127   where $\Delta\varphi$ represents the time change for the parameter of interest (either pCO_2, pH, or Ω_{Ar}), and

128   the four right side terms represent the sDIC, sTA, SSS, and SST contribution to the φ change,

129   respectively. The partial derivatives of the contribution terms were estimated by adding a small

130   perturbation to each driver while keeping the other three terms as constant, using the CO2SYS

131   program for the carbon system calculations.

132   **3 Results**

133   The simulated patterns of surface pCO_2, pH, and Ω_{Ar} anomalies produced basin-averaged

134   trends of 1.57 ± 0.03 µatm yr^{-1}, -0.0015 ± 0.0000 yr^{-1}, and -0.0087 ± 0.0002 yr^{-1} during 1981-

135   2014, respectively. The mean surface pCO_2 trend was somewhat smaller than the growth of

136   atmospheric CO_2, which was at a mean rate of 1.68 µatm yr^{-1} over the same period. Large spatial

137   variability was evident in the modeled trends (Figures 1a–1c; Table S1), suggesting that local

138   processes were influencing the long-term changes. The largest departures from the basin-averaged

139   values were located near the MARS delta, in the central part of the northern GoM shelf, where

140   negative pCO_2 trends and positive Ω_{Ar} and pH trends were obtained nearshore. As a result, the

141   average trend on the northern GoM inner shelf (bottom depth < 25 m; Figure 1f) was 0.93 ± 0.10

142   µatm yr^{-1}, -0.0009 ± 0.0001 yr^{-1} and -0.0003 ± 0.0009 yr^{-1} for pCO_2, pH and Ω_{Ar}, respectively,

143   the slowest rates compared to those in other shelves and the open GoM. The modeled long-term

144   changes in surface pCO_2 impacted the air-sea CO_2 flux (Figure 1d, Table S1). The most prominent

145   feature was on the northern GoM inner shelf, where the CO_2 flux trend was strongly negative

146   (increase in carbon uptake), averaging -0.018 ± 0.003 mol m^{-2} yr^{-2} for a mean flux of -0.844 mol

147   m^{-2} yr^{-1}, but reaching maximum trend magnitude rates greater than -0.050 mol m^{-2} yr^{-2} near the

148   MARS delta. The basin-averaged flux trend was -0.004 ± 0.001 mol m^{-2} yr^{-2} for a model mean

149   flux of -0.382 mol m^2 yr^{-1}.

150   Changes in surface pCO_2, pH, and Ω_{Ar} are connected to changes in DIC, TA, salinity, and

151   temperature. Both pH and Ω_{Ar} increase with TA and decrease with DIC and salinity. However,

152   their response to temperature differs, as warming decreases calcium carbonate solubility

153   (increasing Ω_{Ar}) but promotes hydrogen ion formation (decreasing pH). pCO_2 displays the opposite

154   pattern to that of pH, increasing with DIC, salinity, and temperature, and decreasing with TA. A

155   potential reason for the small pCO_2, pH, and Ω_{Ar} trends on the northern GoM shelf could be an

156   increased biological uptake of DIC that counteracts the DIC increase due to anthropogenic CO_2.

157   However, the simulated surface net community production –the difference between phytoplankton

158   production and community respiration– displayed a weak negative trend near the MARS delta,

159   linked to decreased river discharge and nutrient runoff (Figure 1e). Consequently, a biologically

160   driven offset of the modeled OA trends was discarded.

161   To identify processes responsible for the simulated OA pattern, we examined the Taylor

162   decomposition of the pCO_2, pH, and Ω_{Ar} trends. The patterns showed that sDIC, which had a basin-

163 averaged growth of 1.16 ± 0.02 µmol kg^{-1} yr^{-1}, dominated the total trend variability (Figures 2a–

164 2c; Figure 3a; Table S1). The greatest sDIC impact was on the northern GoM inner shelf, where

165 the sDIC trend was 1.7 times the basin value. This implied that the slow OA progression in the

166 region was not driven by sDIC. Instead, the main process responsible for the slow acidification

167 was a significant sTA growth of 1.90 ± 0.22 µmol kg^{-1} yr^{-1}, which largely counteracted the sDIC-

168 induced changes (Figures 2d–2f; Figure 3b; Table S1). The contributions of SSS and SST to the

169 pCO$_2$, pH, and Ω_{Ar} trends were relatively minor (Figures 2g–2l). The salinity increase, which

170 averaged 0.007 yr^{-1} over the GoM basin and reached values greater than 0.020 yr^{-1} over the

171 northern GoM shelf and the southern part of the West Florida shelf (Figure 3c; Table S1),

172 strengthened the OA pattern. Surface warming, which was 0.008 ± 0.002 °C yr^{-1} on average across

173 the GoM basin (Figure 3d; Table S1), contributed to increase the magnitude of the pH and pCO$_2$

174 trends, and had a weak positive impact on Ω_{Ar}. Although small in magnitude, the SSS and SST-

175 induced changes influenced the spatial OA pattern. If we removed the SSS and SST contribution

176 from the total trends, a smoother trend pattern was obtained (Figure S1).

177 The trend decomposition revealed that sTA played a key role as driver of the simulated OA

178 trends around the MARS delta. Strong sTA growth on the northern GoM shelf, as well as the

179 enhanced sDIC trend, could be linked to changes in MARS chemistry. This was evident when we

180 compared the low-frequency TA and DIC changes for the MARS and the surface northern GoM

181 shelf waters (Figure S2). The TA and DIC from the MARS increased about 5 and 3 µmol kg^{-1} yr^{-}

182 ^{1} during 1981-2014, respectively (Table S2). Declining trends in river discharge (-67 ± 54 m^3 s^{-1}

183 yr^{-1} for the MARS; -53 ± 19 m^3 s^{-1} yr^{-1} for rivers other than MARS) could also contribute to the

184 nearshore sTA and sDIC increase. This is because most rivers along the northern GoM coast,

185 excluding those in the southern and central Texas coast, have relatively low TA and DIC

186 concentration compared to the ocean values; thus, a decreasing discharge implies a reduced

187 influence of the river's dilution effect on these two variables. To quantify the influence of rivers

188 on the ocean carbonate system, we examined the patterns derived from the CLM_RIV and

189 CLM_MC experiments and compared them with the model hindcast. Over the northern GoM shelf,

190 CLM_RIV showed that changes in river discharge and MARS chemistry accounted for 84% of the

191 hindcast sTA trend and 40% of the hindcast sDIC trend (Figures 3e and 3f; Table S3). Over the

192 same region, CLM_MC showed that the MARS chemistry changes (excluding river flow changes)

193 accounted for 61% of the hindcast sTA trend and 32% of the hindcast sDIC trend (Figures S3a and

194 S3b; Table S3). Consequently, changes in river discharge (CLM_MC minus CLM_RIV)

195 accounted for 23% and 8% of the hindcast's TA and DIC trends, respectively (Figures S3e and

196 S3f). Although the sTA trend substantially decreased in the CLM_RIV experiment, a residual TA

197 trend remained across the basin, consistent with a positive trend in SSS (Figure 3g). This sTA and

198 SSS variation, connected to variability in the boundary conditions and a negative trend in

199 precipitation minus evaporation (Figure S4), largely vanished in the CLM_FORC experiment

200 (Figures 3j and 3k).

201   On the northern GoM shelf, the average OA indicators trends in the climatological

202 experiments displayed the same sign than in the hindcast run but with a greater magnitude (Figure

203 4; Table S3). River runoff had a much stronger impact on Ω_{Ar} than on pCO_2 or pH. This was mostly

204 related to the variable's sensitivity to changes in TA and DIC. Ω_{Ar} is slightly more responsive to

205 changes in TA than DIC, whereas pCO_2 and pH are more responsive to changes in DIC than TA

206 (Table S4). Consequently, the DIC-driven changes counteracted to a greater degree the TA-driven

207 changes in the cases of pCO_2 and pH. For other coastal regions and the open GoM, the

208 climatological experiments produced relatively weak trend changes in the OA indicators. At the

209 basin level, the effect of river runoff contributed to reduce the pCO_2, pH, and Ω_{Ar} trends by 5%,

210 6%, and 10%, respectively, while the effect of climate variability contributed to reduce the same

211 trends by 2%, 3%, and 19%, respectively (Figure S5; Table S3). Note that the removal of the

212 surface warming trend in the CLM_FORC experiment (Figure 3l) lessened the growth of pCO_2

213 and the decline of pH, which explained why the strongest pCO_2 and pH trends were obtained by

214 CLM_RIV rather than CLM_FORC.

215 **4 Discussion**

216   High-resolution ocean models are valuable tools to describe OA trends, particularly in the

217 absence of long-term carbon chemistry time-series. In open GoM waters, our model outputs

218 showed surface trends of 1.59 ± 0.02 µatm yr^{-1}, -0.0016 ± 0.0000 yr^{-1}, and -0.0093 ± 0.0001 yr^{-}

219 ^{1} for the mean pCO_2, pH, and Ω_{Ar} anomalies from 1981-2014, respectively. These values are close

220 to previous estimations for subtropical waters in the North Atlantic (Table S5). Along the coastal

221 margins of the GoM, our model revealed significant variations in the OA trend. Estimated shelf

222 averages for the four shelves (Figure 1f) ranged from 1.31 to 1.70 µatm yr^{-1} for pCO_2, from $-$

223 0.0013 to -0.0017 yr^{-1} for pH, and from -0.0042 to -0.0094 yr^{-1} for Ω_{Ar}. For 1996-2018, Kealoha

et al. (2020) reported mean pCO_2 trends of 3.20 ± 1.47 µatm yr^{-1} and 0.08 ± 1.66 on the western and central parts of the northern GoM shelf, and 2.35 ± 0.82 µatm yr^{-1} on the West Florida shelf. The large trend discrepancies between their estimates and ours are most likely due to the limited spatiotemporal coverage of the pCO_2 datasets used by Kealoha et al. (2020), mostly based on underway ship measurements. This limited coverage, added to the large interannual carbon chemistry variability driven by the MARS runoff, determined a large uncertainty to their long-term trend calculations. This also applies to the very strong pCO_2 trend reported in Robbins et al. (2018) for the West Florida shelf (4.37 µatm yr^{-1}).

Although it is expected that CO_2 in the ocean follows the atmospheric CO_2 growth, multiple studies have shown differences between the ocean and atmospheric CO_2 trends, as interannual and interdecadal variability can exert a significant impact on the ocean sink and pCO_2 trend trajectories (McKinley et al., 2020; Bates & Johnson, 2020). Our model results showed that the basin-averaged pCO_2 trend for 1981-2014 was 7% smaller than the historic atmospheric CO_2 trend. Once we removed the effect associated with river runoff in the CLM_RIV experiment, the difference was insignificant (1%). The positive sTA trend had a significant impact on the three OA indicators examined, contributing to lessen OA progression. The largest sTA increase was on the northern GoM shelf associated with MARS chemistry changes, but the model also exhibited positive sTA trends over the open GoM that were not connected to the coastal sTA signature. This result was consistent with observational studies documenting significant alkalinity growth in the subtropical north Atlantic during the last decades (Bates et al., 2014; Bates & Johnson, 2020; Fine et al., 2017). Besides the sTA growth, the model simulated positive trends for SSS and SST. Surface pCO_2 and pH were especially sensitive to SST changes, with surface warming contributing to accentuate the pCO_2 and pH magnitude in trends.

The MARS is a key driver of hydrographic and biogeochemical patterns on the northern GoM shelf. Multiple studies have reported its influence on salinity, coastal circulation, plankton production, nutrients, dissolved oxygen, and carbon chemistry (e.g., Dagg & Breed, 2003; Rabalais et al., 2007; Lohrenz et al., 2012; Huang et al., 2015). Our study adds another aspect to the impact of the MARS runoff, showing that increasing trends in the river alkalinity had a strong buffering effect nearshore. A sensitivity analysis using climatological forced experiments indicated that changes in MARS chemistry accounted for a 42% reduction in the mean surface Ω_{Ar} trend magnitude over the northern GoM shelf. Changes in river discharge further reduced this Ω_{Ar} trend

255 magnitude by 8%. Although the potential for watershed export changes to counteract OA patterns

256 has been long recognized (Provoost et al., 2010; Duarte et al., 2013; Montagna et al., 2018),

257 previous OA studies on the northern GoM shelf have mainly focused on the link between coastal

258 eutrophication and subsurface acidification (e.g., Cai et al., 2011), disregarding the effect of

259 riverine alkalinity changes. Quantifying river runoff impacts on OA trends is difficult due to the

260 lack of observations to describe historical river chemistry changes. We could only prescribe time-

261 evolving TA, DIC, and nutrients concentration for the MARS, which accounts for 80% of the total

262 river discharge in the northern GoM, and climatological TA, DIC, and nutrients for other rivers.

263 Thus, the potential impacts linked to secular chemistry changes in small rivers have not been

264 accurately represented. Although acidification has been suggested for Texas rivers (Hu et al.,

265 2015) several studies have shown that the dominant pattern for the U.S. rivers is alkalinization,

266 linked to agriculture practices such as changes in water fluxes and liming (e.g., Raymond et al.,

267 2008; Kaushal et al., 2013; Stets et al., 2014). Therefore, we could expect that carbon-chemistry

268 trends in small rivers would mostly contribute to strengthening, at a local scale, the simulated sTA

269 trend driven by MARS runoff.

270 **5 Conclusions**

271   Our model results showed significant long-term changes in carbon system patterns across

272 the GoM mainly driven by an increase in atmospheric CO_2. The simulated basin-average patterns

273 in the open GoM were consistent with observational studies of OA in subtropical North Atlantic

274 waters. However, a slow OA progression was found on the northern GoM shelf, associated with a

275 significant increase in sTA. The large sTA trend over the northern GoM shelf was mainly due to

276 a positive trend in MARS alkalinity, and secondarily due to the declining discharge trends of low

277 alkalinity rivers. Our study shows the interplay of multiple processes influencing carbon system

278 variability.

284 assistance with the model experiments, and Emily Osbourne and Gail Derr for their careful
285 manuscript review.

References

294 Bates, N. R., Astor, Y. M., Church, M. J., Currie, K., Dore, J. E., González-Dávila, M., et al.
295   (2014). A time-series view of changing ocean chemistry due to ocean uptake of anthropogenic
296   CO_2 and ocean acidification. *Oceanography*, 27(1): 126–141.

297 Bates, N. R., & Johnson, R. J. (2020). Acceleration of ocean warming, salinification,
298   deoxygenation and acidification in the surface subtropical North Atlantic
299   Ocean. *Communications Earth & Environment*, *1*(1), 1–12.

300 Busch, D. S., Bennett-Mintz, J. M., Armstrong, C. T., Jewett, E. B., Gledhill, D. K., & Ombres, E.
301   H. (2018). NOAA Ocean Acidification Program: Taking Stock and Looking Forward, A
302   summary of the 2017 Principal Investigators' Meeting. U.S. Dept. of Commerce, *NOAA*
303   *Technical Memorandum OAR-OAP-1*, 50 p.

304 Cai, W. J., Hu, X., Huang, W. J., Murrell, M. C., Lehrter, J. C., Lohrenz, S. E., et al. (2011).
305   Acidification of subsurface coastal waters enhanced by eutrophication. *Nature geoscience*,
306   *4*(11), 766–770.

307 Cross, J. N., Turner, J. A., Cooley, S. R., Newton, J. A., Azetsu-Scott, K., Chambers, R. C., et al.
308   (2019). The Knowledge-to-Action Pipeline: Connecting Ocean Acidification Research and
309   Actionable Decision Support. *Frontiers in Marine Science*, *6*, p.356.

310 Dagg, M. J. & Breed, G. A. (2003). Biological effects of Mississippi River nitrogen on the northern
311   Gulf of Mexico–a review and synthesis. *J. Mar. Syst.*, *43*(3-4), 133–152.

312 Damien, P., Pasqueron de Fommervault, O., Sheinbaum, J., Jouanno, J., Camacho-Ibar, V. F., &

313   Duteil, O. (2018). Partitioning of the open waters of the Gulf of Mexico based on the seasonal

314   and interannual variability of chlorophyll concentration. *J. Geophys. Res.-Oceans*, *123*(4),

315   2592–2614.

316   Dee, D. P., Uppala, S. M., Simmons, A. J., Berrisford, P., Poli, P., Kobayashi, S., et al. (2011).

317   The ERA-Interim reanalysis: configuration and performance of the data assimilation system.

318   *Q. J. Roy. Meteor. Soc.,* 137, 553–597.

319   Doney, S. C., Busch, D. S., Cooley, S. R., & Kroeker, K. J. (2020). The Impacts of Ocean

320   Acidification on Marine Ecosystems and Reliant Human Communities. *Annual Review of*

321   *Environment and Resources, 45:*83–112.

322   Doney, S. C., Fabry, V. J., Feely, R. A., & Kleypas, J. A. (2009). Ocean acidification: the other

323   CO2 problem. *Annu. Rev. Mar. Sci.,* 1, 169–92.

324   Duarte, C. M., Hendriks, I. E., Moore, T. S., Olsen, Y. S., Steckbauer, A., Ramajo, L., et al. (2013).

325   Is ocean acidification an open-ocean syndrome? Understanding anthropogenic impacts on

326   seawater pH. *Estuaries and Coasts*, *36*(2), 221-236.

327   Ekstrom, J. A., Suatoni, L., Cooley, S. R., Pendleton, L. H., Waldbusser, G. G., Cinner, J. E., et

328   al. (2015). Vulnerability and adaptation of US shellfisheries to ocean acidification. *Nature*

329   *Climate Change*, *5*(3), 207–214.

330   Fine, R. A., Willey, D. A., & Millero, F. J. (2017). Global variability and changes in ocean total

331   alkalinity from Aquarius satellite data. *Geophysical Research Letters*, *44*(1), 261–267.

332   Gledhill, D. K., Wanninkhof, R., Millero, F. J., & Eakin, M. (2008). Ocean acidification of the

333   greater Caribbean region 1996–2006. *J. Geophys. Res.-Oceans*, *113*(C10).

334   Gomez, F. A., Lee, S. K., Liu, Y., Hernandez Jr, F. J., Muller-Karger, F. E., & Lamkin, J.

335   T. (2018). Seasonal patterns in phytoplankton biomass across the northern and deep Gulf of

336   Mexico: a numerical model study, *Biogeosciences*, 15, 3561–3576.

337   Gomez, F. A., Wanninkhof, R., Barbero, L., Lee, S. K., & Hernandez, F. J. (2020). Seasonal

338   patterns of surface inorganic carbon system variables in the Gulf of Mexico inferred from a

339   regional high-resolution ocean biogeochemical model, *Biogeosciences*, 17, 1685–1700.

340   Gruber, N., Clement, D., Carter, B. R., Feely, R. A., Van Heuven, S., Hoppema, M., et al. (2019).

341   The oceanic sink for anthropogenic CO_2 from 1994 to 2007. *Science*, *363*(6432), 1193-1199.

342   He, B., Kanae, S., Oki, T., Hirabayashi, Y., Yamashiki, Y., & Takara, K. (2011). Assessment of

343   global nitrogen pollution in rivers using an integrated biogeochemical modeling framework.

344   *Water Res.*, 45, 2573–2586.

345   Hoegh-Guldberg, O., Mumby, P. J., Hooten, A. J., Steneck, R. S., Greenfield, P., Gomez, E., et al.
346   (2007). Coral reefs under rapid climate change and ocean acidification. *Science*, *318*(5857),
347   1737–1742.

348   Hu, X., Nuttall, M. F., Wang, H., Yao, H., Staryk, C. J., McCutcheon, M. R., et al. (2018). Seasonal
349   variability of carbonate chemistry and decadal changes in waters of a marine sanctuary in the
350   Gulf of Mexico. *Marine Chemistry*, 205, 16–28.

351   Hu, X., Pollack, J. B., McCutcheon, M. R., Montagna, P. A., & Ouyang, Z. (2015). Long-term
352   alkalinity decrease and acidification of estuaries in northwestern Gulf of Mexico.
353   *Environmental science & technology*, *49*(6), 3401–3409.

354   Huang, W. J., Cai, W. J., Wang, Y., Lohrenz, S. E., & Murrell, M. C. (2015). The carbon dioxide
355   system on the Mississippi River‐dominated continental shelf in the northern Gulf of Mexico:
356   1. Distribution and air‐sea CO2 flux. *J. Geophys. Res.-Oceans*, *120*(3), 1429–1445.

357   Kaushal, S. S., Likens, G. E., Utz, R. M., Pace, M. L., Grese, M., & Yepsen, M. (2013). Increased
358   river alkalinization in the Eastern US. *Environmental science & technology*, *47*(18), 10302–
359   10311.

360   Kealoha, A. K., Shamberger, K. E., DiMarco, S. F., Thyng, K. M., Hetland, R. D., Manzello, D.
361   P., et al. (2020). Surface Water CO_2 variability in the Gulf of Mexico (1996–2017). *Scientific*
362   *reports*, *10*(1), 1–13.

363   Laruelle, G. G., Cai, W. J., Hu, X., Gruber, N., Mackenzie, F. T., & Regnier, P. (2018). Continental
364   shelves as a variable but increasing global sink for atmospheric carbon dioxide. *Nature*
365   *communications*, *9. 454.*

366   Lauvset, S. K., Gruber, N., Landschützer, P., Olsen, A., & Tjiputra, J. F. Trends and drivers in
367   global surface ocean pH over the past 3 decades. *Biogeosciences*, *12*(5), 1285–1298 (2015).

368   Liu, Y., Lee, S. K., Enfield, D. B., Muhling, B. A., Lamkin, J. T., Muller-Karger, F. E., & Roffer,
369   M. A. (2015). Potential impact of climate change on the Intra-Americas Sea: Part-1, A dynamic
370   downscaling of the CMIP5 model projections. *J. Mar. Syst.*, 148, 56–69.

371   Lohrenz, S. E., Cai, W. J., Chakraborty, S., Huang, W. J., Guo, X., He, R., et al. (2018). Satellite
372   estimation of coastal pCO2 and air–sea flux of carbon dioxide in the northern Gulf of Mexico,
373   Remote Sens. Environ., 207, 71–83.

374   Lohrenz, S. E., Cai, W. J., Chen, F., Chen, X., & Tuel, M. (2010). Seasonal variability in air-sea

375   fluxes of CO_2 in a river influenced coastal margin. *J. Geophys. Res.-Oceans*, 115, C10034.

376   Martínez-López, B., & Zavala-Hidalgo, J. (2009). Seasonal and interannual variability of cross-
377   shelf transports of chlorophyll in the Gulf of Mexico. *J. Mar. Syst.*, 77, 1–20.

378   McKinley, G. A., Fay, A. R., Eddebbar, Y. A., Gloege, L., & Lovenduski, N. S. (2020). External
379   forcing explains recent decadal variability of the ocean carbon sink. *AGU Advances*, 1,
380   e2019AV000149.

381   Montagna, P. A., Hu, X., Palmer, T. A., & Wetz, M. (2018). Effect of hydrological variability on
382   the biogeochemistry of estuaries across a regional climatic gradient. *Limnol. Oceanogr.*, *63*(6),
383   2465–2478.

384   Muller-Karger, F. E., Smith, J. P., Werner, S., Chen, R., Roffer, M., Liu, Y., et al. (2015). Natural
385   variability of surface oceanographic conditions in the offshore Gulf of Mexico. *Progress in*
386   *Oceanography*, *134*, 54–76.

387   Muñoz-Salinas, E. & Castillo, M. (2015). Streamflow and sediment load assessment from 1950 to
388   2006 in the Usumacinta and Grijalva Rivers (Southern Mexico) and the influence of ENSO.
389   *Catena*, 127, 270–278.

390   Provoost, P., Van Heuven, S., Soetaert, K., Laane, R. W. P. M., & Middelburg, J. J. (2010).
391   Seasonal and long-term changes in pH in the Dutch coastal zone, *Biogeosciences*, *7*(11), 3869–
392   3878.

393   Rabalais, N. N., Turner, R. E., Gupta, B. S., Boesch, D. F., Chapman, P., & Murrell, M. C. (2007).
394   Hypoxia in the northern Gulf of Mexico: Does the science support the plan to reduce, mitigate,
395   and control hypoxia?. *Estuaries and Coasts*, *30*(5), 753–772.

396   Raymond, P. A., Oh, N. H., Turner, R. E., & Broussard, W. (2008). Anthropogenically enhanced
397   fluxes of water and carbon from the Mississippi River. *Nature*, *451*(7177), 449–452.

398   Robbins, L. L., Daly, K. L., Barbero, L., Wanninkhof, R., He, R., Zong, H., et al. (2018). Spatial
399   and temporal variability of pCO_2, carbon fluxes and saturation state on the West Florida Shelf.
400   *J. Geophys. Res.-Oceans*, 123.

401   Salisbury, J. E., & Jönsson, B. F. (2018). Rapid warming and salinity changes in the Gulf of Maine
402   alter surface ocean carbonate parameters and hide ocean acidification. *Biogeochemistry*,
403   *141*(3), 401–418.

404   Shchepetkin, A. F., & McWilliams, J. C. (2005). The regional oceanic modeling system (ROMS):
405   a split-explicit, free-surface, topography-following-coordinate oceanic model. *Ocean Model.*,

406   9, 347–404.

407   Stets, E. G., Kelly, V. J., & Crawford, C. G. (2014). Long-term trends in alkalinity in large rivers

408   of the conterminous US in relation to acidification, agriculture, and hydrologic modification.

409   *Sci. Total Environ.*, 488, 280–289.

410   Turi, G., Lachkar, Z., Gruber, N., & Münnich, M. (2016). Climatic modulation of recent trends in

411   ocean acidification in the California Current System, *Environmental Research Letters*, *11*(1),

412   p.014007.

413   van Heuven, S. M. A. C., Pierrot, D., Rae, J. W. B., Lewis E., & Wallace D. W. R. (2011).

414   MATLAB program developed for CO2 system calculations. ORNL/CDIAC-105b. Carbon

415   Dioxide Information Analysis Center, Oak Ridge National Laboratory, US Department of

416   Energy, Oak Ridge, Tennessee, 530.

417   Waldbusser, G. G., Hales, B., Langdon, C. J., Haley, B. A., Schrader, P., Brunner, E. L., et al.

418   (2015). Saturation-state sensitivity of marine bivalve larvae to ocean acidification. *Nature

419   Climate Change*, *5*(3), 273–280.

420   Wang, Z. A., Wanninkhof, R., Cai, W. J., Byrne, R. H., Hu, X., Peng, T. H., & Huang, W. J.

421   (2013). The marine inorganic carbon system along the Gulf of Mexico and Atlantic coasts of

422   the United States: Insights from a transregional coastal carbon study. *Limnol. Oceanogr.*, 58,

423   325–342.

424   Wanninkhof, R., Barbero, L., Byrne, R., Cai, W. J., Huang, W. J., Zhang, J. Z., et al. (2015). Ocean

425   acidification along the Gulf Coast and East Coast of the USA. *Continental Shelf Research*, 98,

426   54–71.

427   Wanninkhof, R., Trinanes, J., Park, G.-H., Gledhill, D., & Olsen, A. (2019). Large decadal changes

428   in air-sea CO_2 fluxes in the Caribbean Sea. Journal of Geophysical Research: Oceans, 124,

429   6960–6982, https://doi.org/10.1029/2019JC015366

430   Xu, Y. Y., Cai, W. J., Wanninkhof, R., Salisbury, J., Reimer, J., & Chen, B. (2020). Long-term

431   changes of carbonate chemistry variables along the north American East Coast. *J. Geophys.

432   Res.-Oceans: Oceans*, *125*(7), 2019JC015982.
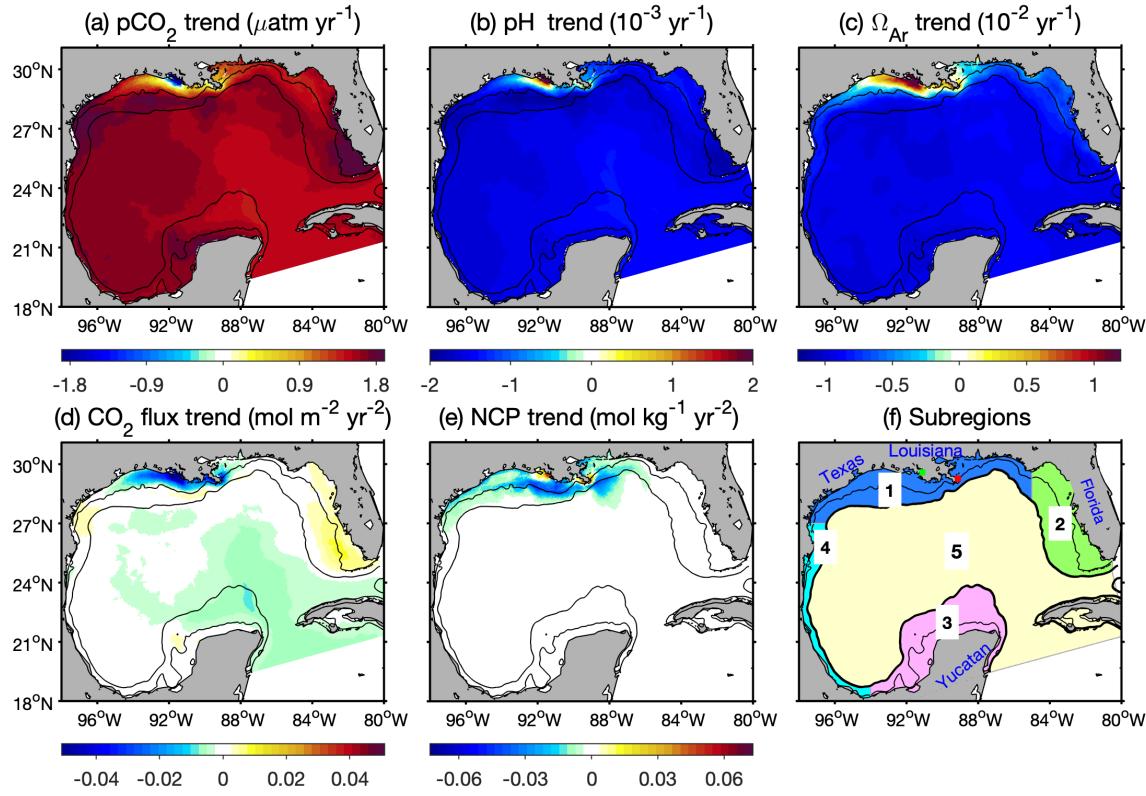
Figure 1. Surface trends of (**a**) partial pressure of CO_2, (**b**) pH, **c**) aragonite saturation state, (**d**) air-sea CO_2 flux, and (**e**) net community production derived from the model hindcast. (**f**) Areas used to derive subregional trend patterns: (1) northern GoM shelf; (2) West Florida shelf; (3) Yucatan shelf; (4) western GoM shelf; and (5) open GoM. Red and green dots in (f) depict the Mississippi and Atchafalaya mouths, respectively. Negative CO_2 flux trend implies increasing carbon uptake. Black contours depict the 25 and 200 m isobaths. The 25 m isobath defines the limit between the inner and outer shelf.
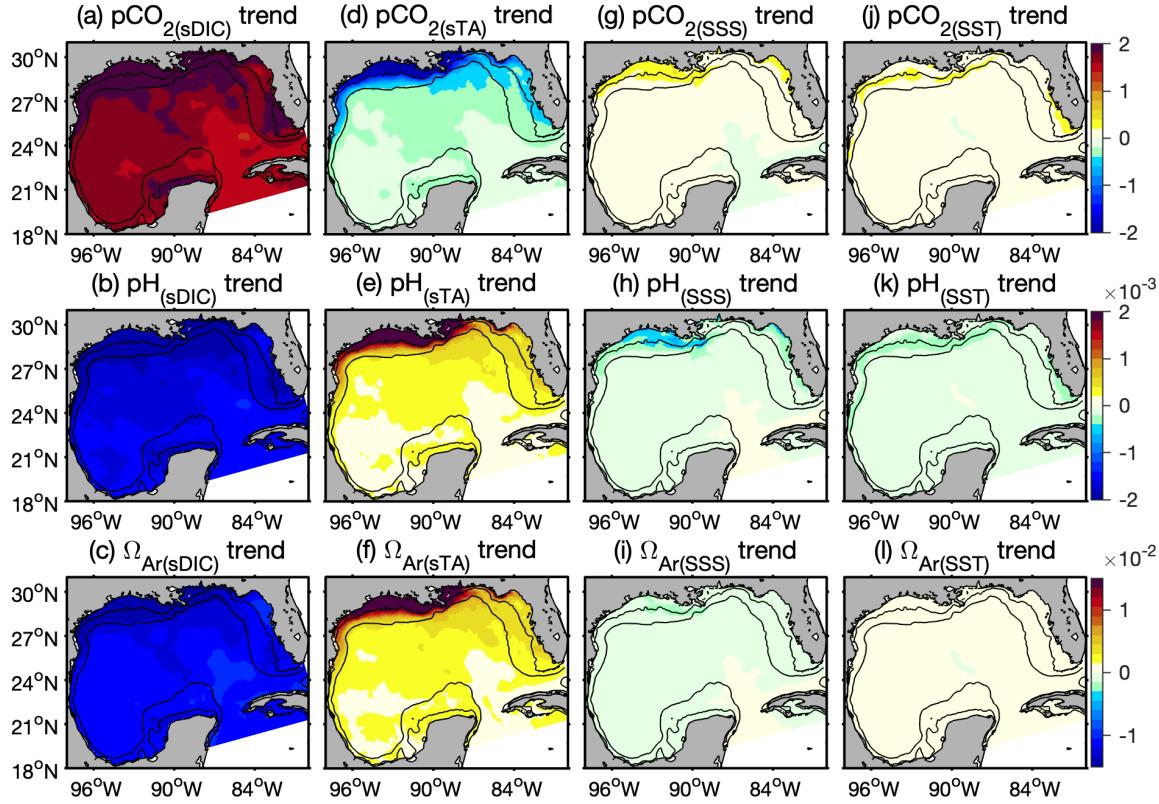
Figure 2. Taylor series decomposition of the surface partial pressure of CO_2 (μatm yr^{-1}; upper panels), surface pH (yr^{-1}; middle panels), and surface aragonite saturation state (yr^{-1}; bottom panels) trends derived from the model hindcast. Patterns terms represent the contribution of **(a–c)** surface dissolved inorganic carbon (sDIC); **(d–f)** surface total alkalinity (sTA); **(g–i)** sea surface salinity (SSS); and **(j–l)** sea surface temperature (SST). Black contours depict the 25 and 200 m isobaths.
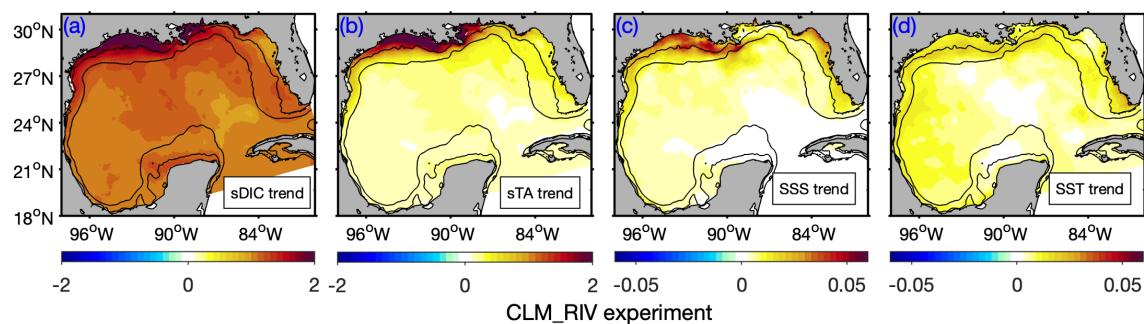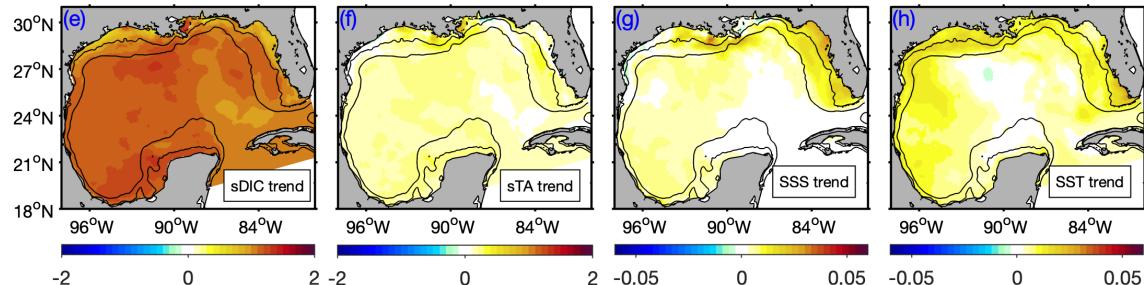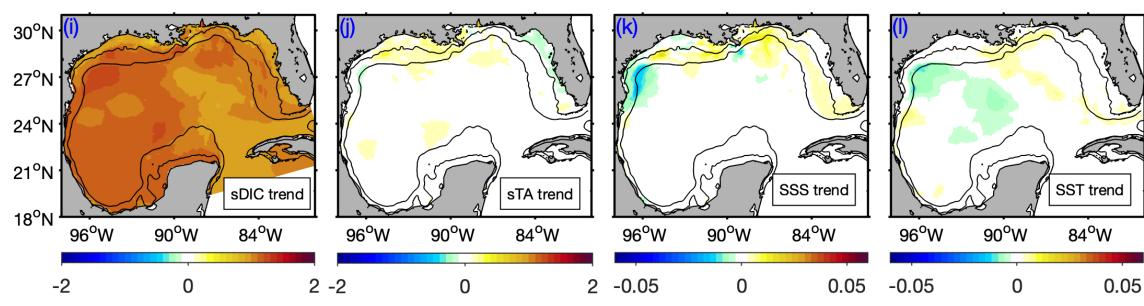
Figure 3. Trends of surface dissolved inorganic carbon (sDIC), surface total alkalinity (sTA), sea surface salinity (SSS), and sea surface temperature (SST) as derived from the **(a–d)** hindcast, **(e–h)** climatological rivers (CLM_RIV), and **(i–l)** climatological forcing (CLM_FORC) experiments. Trends for sDIC and sTA are in µmol kg^{-1} yr^{-1}, for SSS in yr^{-1}, and for SST in °C yr^{-1}. Black contours depict the 25 and 200 m isobaths.
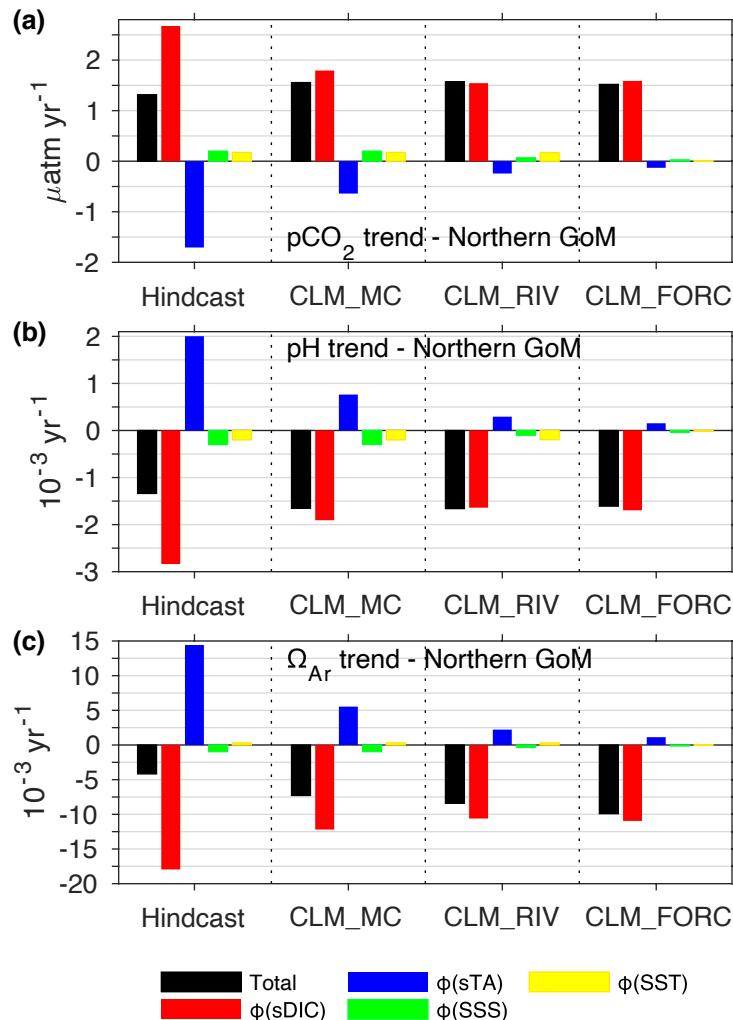
Figure 4. Trend decomposition of ocean acidification indicators over the northern GoM shelf derived from the hindcast, CLM_MC, CLM_RIV, and CLM_FORC experiments: **(a)** partial pressure of CO_2 **(pCO2)**, **(b)** pH, and **(c)** aragonite saturation state (Ω_{Ar}**).** Red, blue, green, and yellow bars represent the contribution of surface dissolved inorganic carbon (sDIC), surface total alkalinity (sTA), sea surface salinity (SSS), and sea surface temperature (SST) to the total trend (in black), respectively.